processes

MDPI

Article

Analysis of Dynamic Load Characteristics of Accelerated Pavement Testing Equipment Based on Virtual Prototype Model

Hailu Yang [1], Xiaohui Huang [1], Zhoujing Ye [1], Linbing Wang [2,*] and Fengyan Sun [1,*]

[1] National Center for Material Service Safety, University of Science and Technology Beijing, Beijing 100083, China; yanghailu@ustb.edu.cn (H.Y.); huangxiaohui97@163.com (X.H.)
[2] College of Engineering, University of Georgia, Athens, GA 30602, USA
* Correspondence: linbing.wang@uga.edu (L.W.); fysun@ustb.edu.cn (F.S.)

Abstract: The purpose of this paper is to study the actual dynamic load characteristics of a full-scale Accelerated Pavement Test (APT) device called Natural Environment-Automatically Loaded Track (NE-ALT) during its operation. The NEALT uses hydraulic and support reaction forces to apply axle loads, which are somewhat different from real trucks. Therefore, in order to ensure the accuracy of the loading parameters of the device, it is necessary to analyze the dynamic load characteristics of the device during operation. In this paper, a virtual prototype model of the device was established, and the important parameters, including vehicle speed and axle load, were set. The dynamic axle load, dynamic load coefficient, and influential factors of the NE-ALT were analyzed using the model at different speeds, hydraulic pressures, and road roughness. The results have shown that the dynamic axle load accuracy was most affected by speed, followed by road roughness, and then hydraulic cylinder pressure. Compared with the real truck, its dynamic load stability was better than the real truck due to the restriction of the guide rail in the acceleration loading system and the method of hydraulic loading, and the larger the load, the more stable the load, which was different from the real truck. Therefore, in the design of accelerated pavement loading experiments, the dynamic axle load characteristics of equipment need to be considered. The results of this study can provide guidance for the further improvement and application of the NE-ALT.

Keywords: accelerated pavement test; dynamic axle load; multi-body dynamics; simulation

Citation: Yang, H.; Huang, X.; Ye, Z.; Wang, L.; Sun, F. Analysis of Dynamic Load Characteristics of Accelerated Pavement Testing Equipment Based on Virtual Prototype Model. *Processes* **2023**, *11*, 1239. https://doi.org/10.3390/pr11041239

Academic Editor: Haiping Zhu

Received: 20 March 2023
Revised: 8 April 2023
Accepted: 12 April 2023
Published: 17 April 2023

1. Introduction

During the driving of a vehicle, due to the influence of road roughness, dynamic tire force is generated by vehicle-pavement interaction [1]. The combination of the dynamic tire force and the static axle load forms the actual dynamic axle load force acting on the road. The dynamic axle load is constantly fluctuating and is one of the important factors that cause road damage. Regarding the dynamic load impact on the road, researchers in vehicle engineering focus on the changes in vehicle dynamic axle load under different working conditions and the measurement of vehicle dynamic axle load [2–6]. Lu et al. [7] studied the influence of vehicle speed, load, road roughness, and tire stiffness on the dynamic axle load and Dynamic Load Coefficient (*DLC*) based on the heavy-duty vehicle DFL1250A9. Buhari et al. [8] compared the influence of air spring suspension and leaf spring suspension on the dynamic load coefficient of the vehicle. Lin [9] proposed a spectrum method to study the influence of road roughness and vehicle speed on dynamic axle load. Ka'Ka et al. [10] used the mechanism of vehicle wheel suspension to calculate the actual vehicle dynamic axle load on the road. Researchers in road engineering focus on road damage under different vehicle dynamic axle loads [11–14]. Rys [15] studied the main reasons for road damage caused by dynamic axle load under different vehicle speed conditions. Mshali and Steyn [16] studied the elastic surface deflection of different flexible road sections under dynamic axle load. Ye et al. [17] studied the effect of random non-uniform loads

on dynamic pavement response by comparing the pavement responses under constant non-uniform load and constant uniform load. Yan et al. [18] conducted research on the road acceleration field under dynamic axle load.

Rutting is one of the significant distresses in flexible pavements, and Joumblat et al. [19] summarized the research about the permanent deformation characterization of asphalt concrete pavements. Accelerated Pavement Testing (APT) is an efficient method for studying pavements in road engineering. Researchers have conducted extensive research on pavement materials based on various accelerated pavement test devices [20–24]. John Harvey et al. [25,26] studied the rutting and cracking performance of asphalt rubber and conventional asphalt concrete overlay using an APT device. Yang et al. [27] analyzed the effect of vehicle loading speed on the permanent deformation of road surface through APT and numerical simulation. Dragoș Ungureanu et al. [28] adopted APT to test a recycled road structure made with reclaimed asphalt pavement material. Li et al. [29] tested and studied recycled asphalt pavement using APT equipment. Jiang et al. [30] Evaluated the performance of inverted pavement structures using APT. However, in these studies, the static axle load is directly used to analyze the asphalt pavement structure and materials, and the actual dynamic axle load of the device itself is not analyzed and studied. The direct equivalent of the dynamic axle load of the device to the static axle load will inevitably lead to errors in the calculation results. Therefore, it is necessary to analyze the dynamic axle load of the accelerated pavement test device. The "Special Region Environment Structural Material Test Device" project independently developed the Natural Environment-Automatically Loaded Track (NE-ALT) and the Controlled Environment-Multi-axle Loading Facility (CE-MLF). The main feature of the NE-ALT is the use of the truck rear suspension assembly, which accurately sets the axle load through hydraulic loading, and conducts the test on the ring test road. The ring test road includes straight sections and semicircular sections. The running path of the device is guided and restricted by the guiding tracks on both sides of the road. Wang et al. [31] used this device to study the dynamic responses of asphalt pavement in dry and saturated conditions under full-scale accelerated loading and verified the reliability of the device.

This study utilized multi-body dynamics analysis software ADAMS to construct a virtual prototype model of the NE-ALT and verified its reliability through various methods. Based on the virtual prototype model, simulation experiments were conducted to analyze different factors that affect the dynamic load characteristics of the device, and the results were compared with those of the actual vehicle under the same operating conditions. This research has identified that the Dynamic Load Coefficient *DLC* of NE-ALT varies with different speeds and road roughness, which is similar to the actual vehicle. However, it is affected by different axle loads, and the change law is the opposite. This study provides an understanding of the differences in dynamic loading characteristics between the device and actual trucks.

2. Evaluation Indicators and Methods

2.1. Dynamic Axle Load Characteristic Evaluation Indicators

In the study of dynamic axle load characteristics of a vehicle, researchers have proposed a variety of evaluation indicators. Cebon [32] proposed the Dynamic Load Coefficient *DLC*, and Zhang et al. [33] proposed the Impact Factor *IM*. These indicators can reflect the degree of road damage caused by dynamic axle load to a certain extent. This study uses the most widely used *DLC* and *IM* as evaluation indicators to study the dynamic axle load characteristic of the NE-ALT.

(1) Dynamic Load Coefficient *DLC*

DLC reflects the violent fluctuation of the dynamic axle load on the entire section with the static axle load as the center and is defined as Equation (1) (by Cebon 1986 [32]).

$$DLC = \frac{1}{F_s}\sqrt{\frac{\sum_{i=1}^{N}(F_i - F_s)^2}{N-1}} \times 100\% \quad (1)$$

where: F_i is the dynamic axle load at the ith time step, F_s is the static axle load; N is the total time step.

(2) Impact factor *IM*

IM reflects the percentage increase of dynamic load relative to the static load and characterizes the extreme change of the dynamic load. It is defined as Equation (2).

$$IM(\%) = \left(\frac{F_t}{F_s} - 1\right) \times 100\% \quad (2)$$

where: F_t is the maximum dynamic axle load of the vehicle, and F_s is the static load.

2.2. Establishment of Virtual Prototype Model

With the development of multi-body system dynamics analysis software represented by ADAMS and SIMPACK, the establishment of virtual prototype models in such software to reflect the complex structural characteristics of vehicles has been widely used in vehicle dynamics research [34,35]. This study uses ADAMS as the multi-body dynamics analysis software to establish the virtual prototype model of the NE-ALT.

The overall structure of the Natural Environment-Automatically Loaded Track (NE-ALT is shown in Figure 1a. The NE-ALT is composed of a loading system, a constrained track system, a power supply system, a loop test road system, a control system, a hydraulic pump station, and a sound barrier. In the construction process of the NE-ALT multi-body dynamic model, due to the limited impact of the dynamic performance of the power supply device, it is generally omitted. The hydraulic pump station and control cabinet can be simplified as counterweights. Sound barriers can be omitted. Therefore, the operational entities of NE-ALT can be simplified as loading systems, constrained track systems, and loop test road systems, as shown in Figure 1b. The accelerated loading system is mainly composed of the loaded vehicle body and the truck rear suspension assembly; the constrained track system is composed of double-sided steel tracks; the test road system is a highway pavement structure typical in Changping District, Beijing.

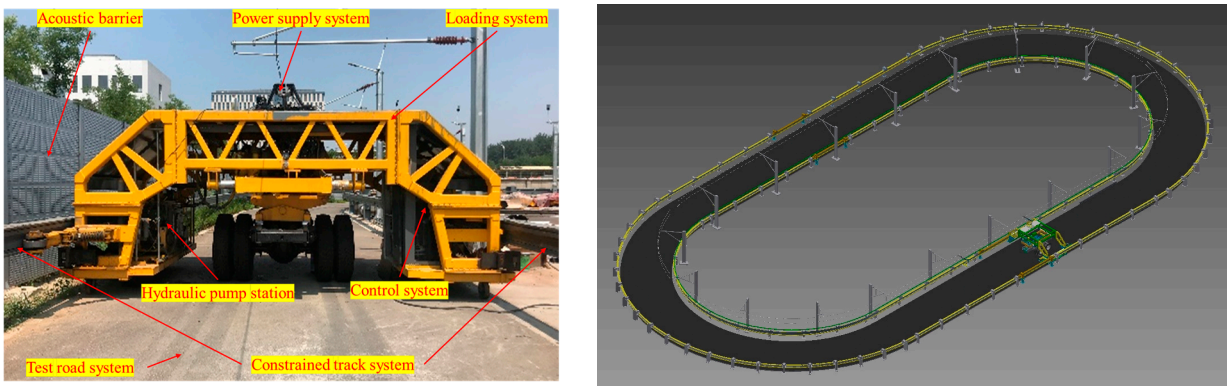

(**a**) (**b**)

Figure 1. Natural Environment-Automatically Loaded Track. (**a**) Partial view of NE-ALT. (**b**) Assembly drawing of NE-ALT.

The NE-ALT is driven by a DC drive motor with a vehicle speed adjustment range of 0–30 km/h. The loading unit adopts the axle of a real heavy-duty truck and applies the load through hydraulic, with an axle load adjustment range of 200–280 kN. There are two types of loaded wheel axle combinations: single axle 4 wheels and dual axle 8 wheels. The lateral swing distance of the axle is ±250 mm. The constrained track adopts a dual-sided steel track structure, providing guidance and loading reaction force support for the device. The power supply system adopts a pantograph network contact power supply. The device detection signal is transmitted by the wireless transmission system to the upper computer for remote control. This system can achieve automatic high-speed cyclic loading of various

road materials and structures, with functions of variable load and adjustable speed. The NE-ALT controllable parameters are the motor speed and the hydraulic pressure, which correspond to the vehicle speed and axle total load, respectively.

The total length of the test road is about 187 m, which is composed of two 40 m long straight sections used as the testing road section and two arc road sections with a radius of 17 m. The width of the test road is 6 m.

The guiding philosophy is to make the virtual prototype model not only convenient to establish and improve but also accurately simulate the actual condition. Therefore, the model was divided into a track model formed by the combination of the test road system and the operating track system; the loaded vehicle body model used to analyze the wheel/track contact; and the rear suspension model for analyzing tire/road contact with heavy truck rear suspension assembly as the main body.

The contact relationship among the three sub-models mainly includes the wheel/track contact of each wheel installed on the loaded vehicle body sub-model with the inner and outer tracks of the operating track model and the tire/road contact between the tires of the rear suspension sub-model and the road surface of the operating track sub-model. The contact relationship of the sub-model is shown in Figure 2.

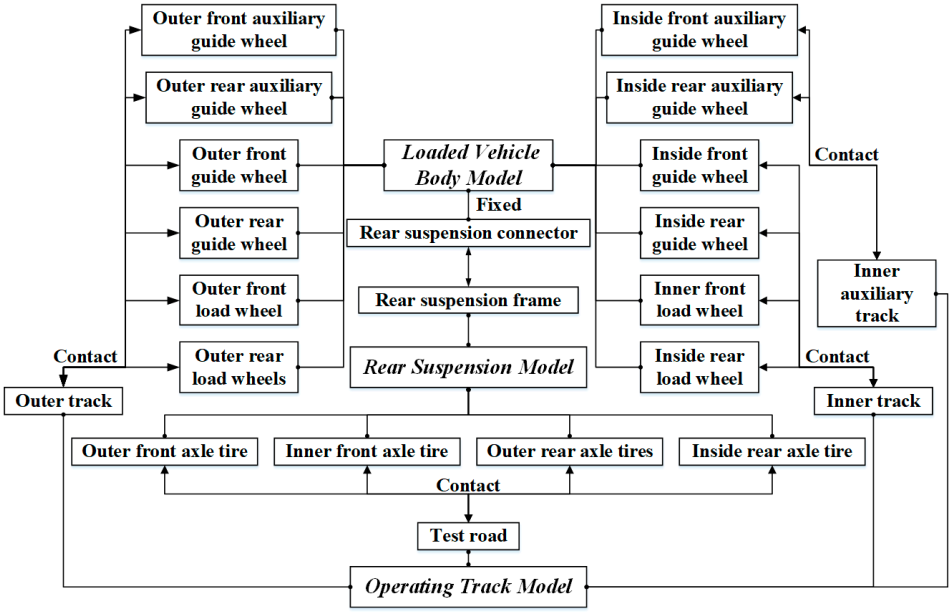

Figure 2. The relationship of sub-models of NE-ALT.

According to Figure 2, by adding constraints and contacts between the sub-model components, the virtual prototype model shown in Figure 3 can be obtained in ADAMS.

Constructing an accurate tire/road contact relationship is the key to accurately reflecting the dynamic axle load characteristics of the device. In the virtual prototype model, the tire model "magic formula" proposed by Pacejka [36] was used to construct the tire model, which had good robustness, and if there was no test data for a certain tire, it could still achieve good results with similar tire data substitution. Based on the magic formula, the force change of the tire during operation can be obtained.

$$Y(x) = Dsin\{\text{Carctan}[Bx - N(Bx - \arctan(Bx))]\} \quad (3)$$

where, $Y(x)$ is the tire's lateral force, longitudinal force, or torque; x is the tire's side slip angle α or longitudinal slip rate λ; D is the peak factor; C is the form factor; B is the stiffness factor; N is the curvature factor.

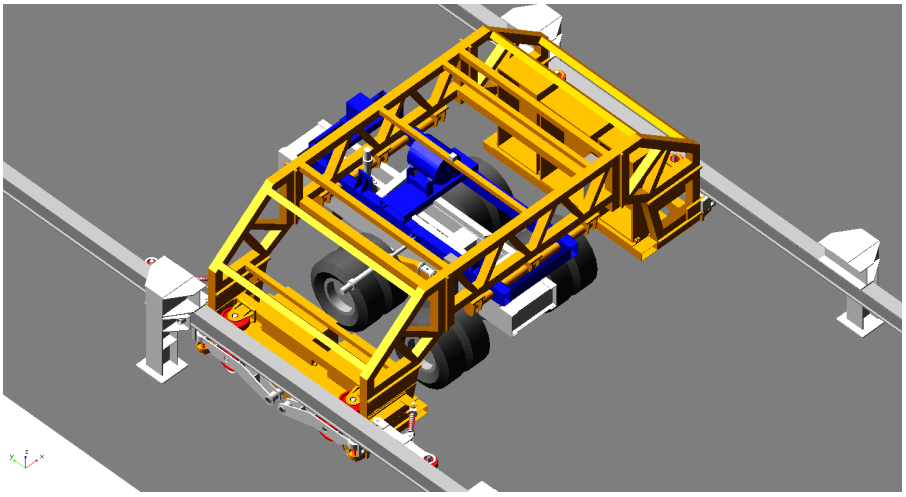

Figure 3. Virtual prototype model of NE-ALT.

In this study, the main analysis is the force state of the tire on the experimental road section, which is a straight road section. On the straight road section, the longitudinal force F_{x0} of the device was calculated with the input variable being slip rate λ and the vertical load F_z. The formula is:

$$F_{x0}(\lambda) = D_x \sin\{C_x \arctan[B_x\lambda - N_x(B_x\lambda - \arctan(B_x\lambda))]\} \tag{4}$$

where, $D_x = a_1F_Z^2 + a_2F_Z$; $C_x = 1.65$; $B_x = \left[\left(a_3F_Z^2 + a_4F_Z\right)e - (a_5F_Z)\right]/(C_xD_x)$; $N_x = a_6F_Z^2 + a_7F_Z + a_8$; a_i is the fitting coefficient with the value [−21.3, 1144, 49.6, 226, 0.069, −0.006, 0.056, 0.486].

The curved road section needs to calculate the longitudinal force F_x of the device and the lateral force F_y of the device at the same time, and the input variables are the slip rate λ, the lateral declination angle α, and the vertical load F_z.

$$F_x = \frac{\eta_x}{\eta}F_{x0} \tag{5}$$

where, $\eta = \sqrt{{\eta_x}^2 + {\eta_y}^2}$; $\eta_x = -\frac{\lambda}{1+\lambda}$; $\eta_y = -\frac{\tan\alpha}{1+\lambda}$.

The lateral force formula for the curved road segment is:

$$\begin{cases} F_y = \frac{\eta_y}{\eta}F_{y0} \\ F_{y0}(x) = D_y \sin\{C_y \arctan[B_yx - N_y(B_yx - \arctan(B_yx))]\} + S \\ x = \alpha + S_h \end{cases} \tag{6}$$

where, $D_y = b_1F_Z^2 + b_2F_Z$; $C_y = 1.3$;
$B_y = \{b_3 \sin[b_4 \arctan(b_5F_z)](1 - b_{12}|\gamma|)\}/(C_yD_y)$;
$E_y = b_6F_Z^2 + b_7F_Z + b_8$;
$S_h = b_9\gamma$, S_h is the horizontal drift;
$S_v = (b_{10}F_Z^2 + b_{11}F_Z)\gamma$, S_v is the vertical drift;
γ is the tire roll angle;
$[b_1, \ldots, b_{12}]$ = [−22.1, 1011, 1078, 1.82, 0.208, 0, −0.354, 0.707, 0.028, 0, 14.8, 0.022].

In the ADAMS, selecting the magic formula based "pac2002_315_80R22_5" tire model file serves as the tire model for the simulation model. By inserting the center point of the self-built tire model into the tire model and adding rotational constraints to the device axle, the force changes during operation can be obtained from the tire model.

In vehicle engineering, road roughness is usually described according to the Power Spectral Density (*PSD*) of the road surface. The virtual prototype model road surface model can be directly set as the two-dimensional simplified road surface of different classes under

the *PSD* standard. Meanwhile, the leaf spring suspension model has a certain influence on the dynamic axle load characteristics. Shi [37] conducted relevant research on the rear axle suspension of heavy trucks, and the leaf spring model was established by using discrete beams.

PSD in ADAMS characterizes pavement *IRI* parameters. Using the pavement surface as a reference plane, the two-dimensional simplified pavement corresponding to the Class A pavement standard is set up, and the pavement tire relationship model is established.

2.3. Validation of the Virtual Prototype Model

2.3.1. Validation of Speed Control Parameters

In the virtual prototype model, the different speeds and axle loads in the simulation are obtained by controlling the tire speed and hydraulic cylinder pressure. Therefore, it is necessary to correct the control parameters first, then verify the dynamic axle load changes during the operation and measure the road roughness.

The tire speed calculation formula in the simulation model is shown as Equation (7).

$$n_w = \alpha \times n_m \times i_m \times i_t \times i_v \times \eta \tag{7}$$

where α is the transmission correction coefficient; n_m is the motor speed; i_m is the transmission ratio of the motor gearbox; i_t is the transmission ratio of the transmission system; i_v is the axle system transmission ratio; η is the mechanical transmission efficiency.

In the experiment, the hydraulic system was controlled to achieve a total axle load of approximately 224 kN, corresponding to a hydraulic pressure of 10 MPa. Under this axle load condition, the motor speed was controlled to accelerate from 200 r/min to 800 r/min.

Piezoelectric sensors and acceleration sensors embedded in the road were used to obtain the interval between the voltage peaks generated by the device's front and rear axles passing. The laser rangefinder was used to obtain the interval time between two passes of the laser rangefinder. These two kinds of time intervals were calculated with wheelbase and test road length, respectively, to obtain the corresponding relationship between motor speed and vehicle speed, which is shown in Figure 4.

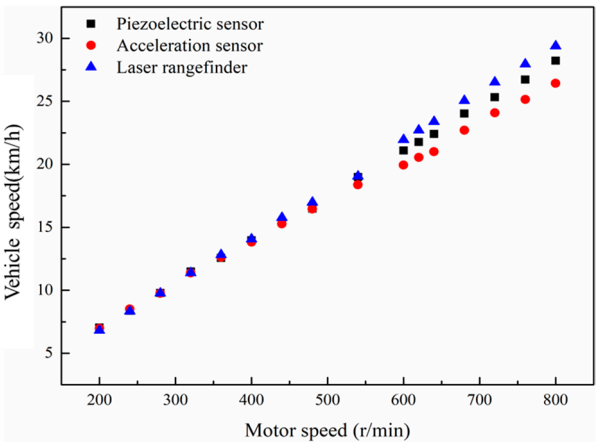

Figure 4. Relation between motor speed and device speed.

The measured speed and the simulated speed under the same motor speed are compared in Table 1. It can be seen from the table that the simulated value is slightly higher than the measured value. The main reason is that the simulation model did not consider the wind resistance and torque transmission loss in actual operation. However, the maximum relative error is 1.81%, indicating that the simulated speed in the simulation model can match the measured speed well.

Table 1. Comparison of measured and simulated speeds.

Motor Speed/(r/min)	Measured/(m/s)	Simulated/(m/s)	Relative Error
310	2.93	2.98	1.67%
410	4.16	4.20	1.03%
510	5.58	5.62	0.67%
610	6.91	6.98	1.07%
710	8.28	8.43	1.81%

2.3.2. Validation of Static Axle Load Control Parameters

Hydraulic cylinder loading force F_h in the virtual prototype model is calculated by Equation (8).

$$F_h = \beta P \times \pi \times r^2 \tag{8}$$

where β = 1.16 is the pressure proportional coefficient; P is the hydraulic circuit input pressure; r = 40 mm is the loading hydraulic cylinder radius.

The HLDB portable dual-axis axle load detector shown in Figure 5 is used to measure the static axle load of the device.

Figure 5. Static axle load measurement of NE-ALT.

The device realizes the adjustment of the axle load by controlling the pressure of the hydraulic cylinder, and the pressure adjustment range is 8~12 MPa. The composition of the device's loading system is shown in Figure 6.

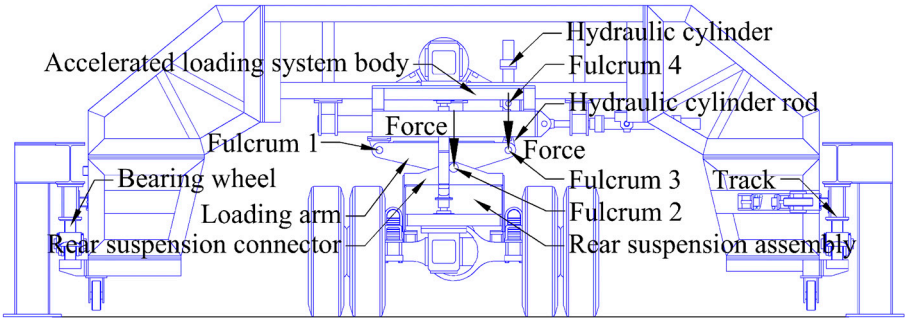

Figure 6. Loading System of NE-ALT.

Two hydraulic cylinders are respectively installed on the front and rear sides of the accelerated loading system and are connected to the body of the device through fulcrum 4. The top of the hydraulic cylinder rod is connected to fulcrum 3 with the loading arm, and the loading arms at both ends are connected by H-shaped steel. The loading arm and the rear suspension connector are connected by fulcrum 2, and the rear suspension connector is connected to the rear suspension assembly by bolts. When the hydraulic cylinder is

loaded, the force is transmitted from the top of the hydraulic cylinder rod to the loading arm through fulcrum 3. The loading arms have a tendency to rotate around fulcrum 1 in order to maintain the force balance of the loading arms, fulcrum 2 gives the loading arms force, and the reaction force will eventually be transmitted to the rear suspension assembly. At the same time, the force received by the hydraulic cylinder will be transmitted to the body of the accelerated loading system through fulcrum 4, and the body will transmit the force to the track through the four bearing wheels contacting the lower surface of the track.

The pressure of the hydraulic cylinder was taken at 0.5 MPa intervals, and the measurement results are shown in Figure 7.

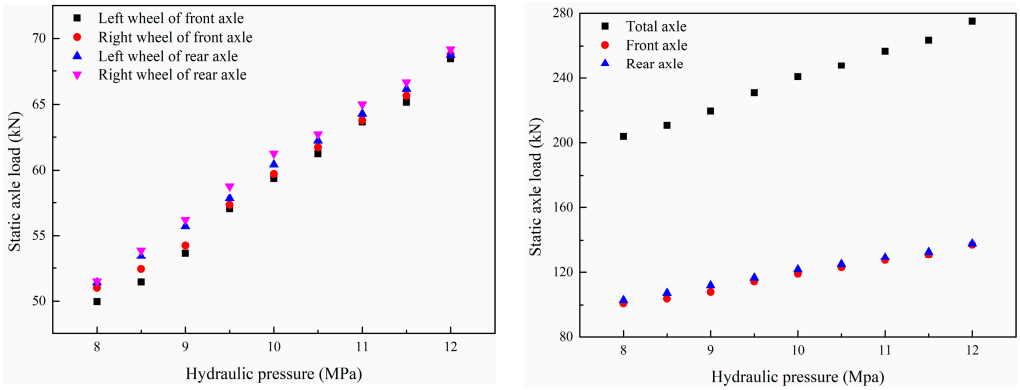

(**a**) (**b**)

Figure 7. Relation between the hydraulic pressure and static axle load. (**a**) Load of each tire. (**b**) Each axle and total axle.

In the virtual prototype model, the pressure of the hydraulic cylinder was selected as 8 MPa, 9 MPa, 10 MPa, 11 MPa, and 12 MPa. Table 2 is obtained by comparing the simulated static axle load with the measured static axle load.

Table 2. Comparison of measured and simulated axle load.

Hydraulic Pressure (MPa)		Front Axle (kN)	Rear Axle (kN)	Total Axle (kN)
Measured	8	100.98	102.91	203.90
Simulated		102.60	100.72	203.32
Relative error		1.58%	−2.17%	−0.29%
Measured	9	107.95	111.93	219.86
Simulated		112.47	110.54	223.21
Relative error		4.02%	−1.26%	1.50%
Measured	10	119.12	121.72	240.84
Simulated		122.34	120.37	242.70
Relative error		2.63%	−1.12%	0.77%
Measured	11	128.04	128.85	256.89
Simulated		132.05	130.25	262.29
Relative error		3.04%	1.07%	2.06%
Measured	12	137.27	138.08	275.35
Simulated		142.03	139.99	282.03
Relative error		3.35%	1.36%	2.37%

Comparing the measured data with the simulated, it can be seen that the relative error of the total static axle load of the device does not exceed 2.37%, and the maximum deviation of the single-axis static axle load does not exceed 4.02%. Due to the large axle load value, there may be certain errors in actual measurement and simulation calculation, but in general, the deviation value of each wheel is within the allowable range, which can

ensure that the tire force in the simulation model can be used to simulate the axle load of the device.

2.3.3. Measurement of Dynamic Axle Load

The road dynamic weighing system based on piezoelectric sensors developed by Zhao et al. [38], as shown in Figure 8, was embedded in the test road, which can be used for the dynamic weighing test of the device. In order to avoid the influence of irrelevant variables, the buried position of the piezoelectric sensors was selected on the road section where the speed is stable, and the road roughness changes closest to the average value.

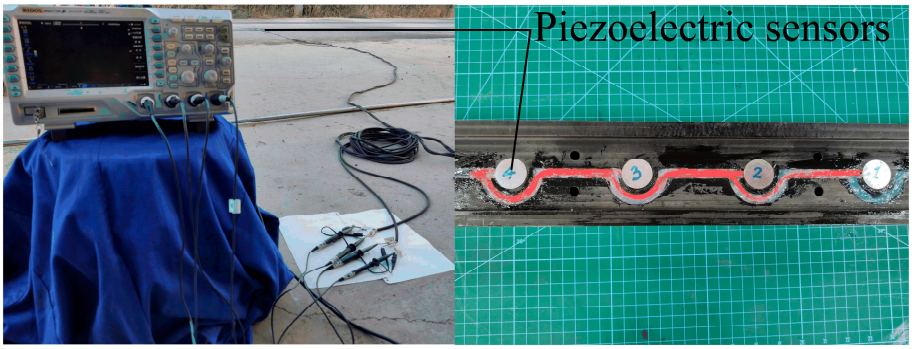

Figure 8. Road dynamic weighing system.

In applying this dynamic weighing system, the speed of the device was controlled between 6.98~20.55 km/h, and the pressure of the hydraulic cylinder was controlled to 9 MPa. The system obtains the piezoelectric sensor voltage amplitude changes when the front and rear axles pass through the system at different speeds. In this experiment, the vehicle speed was set to 10 km/h in order to ensure the stable operation of the device; the pressure of the hydraulic cylinder was controlled between 8.5 and 10.5 MPa, and the voltage amplitude of the piezoelectric sensor was obtained when the front and rear axles of the device pass through the system under different pressure conditions. Compared with the measured static axle load, the *DLC* changes of the device under different hydraulic pressures and different speeds are shown in Figure 9.

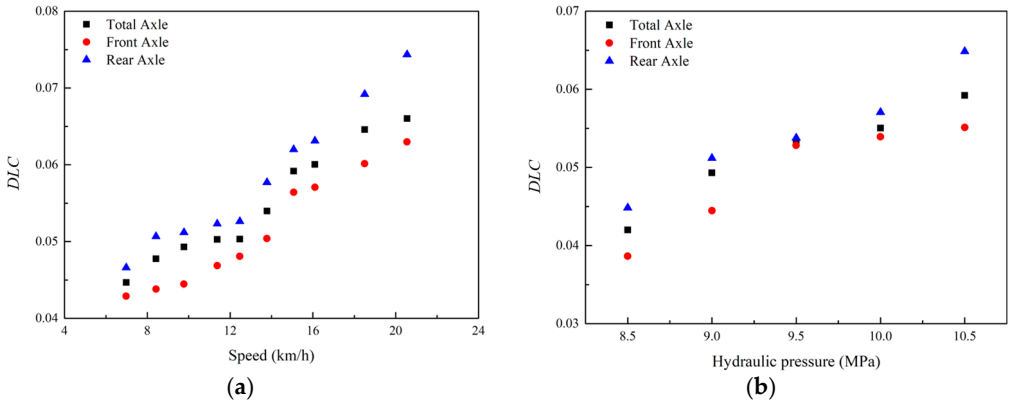

Figure 9. Measurement of dynamic axle load. (**a**) Relationship between *DLC* and speed. (**b**) Relationship between *DLC* and hydraulic pressure.

It can be seen from the above figure that the *DLC* increases as the vehicle speed increases. When the vehicle speed increases from 6.98 km/h to 20.55 km/h, the *DLC* increases from about 0.045 to 0.066.

The general rule of vehicle *DLC* changing with axle load is that the two are in a negative correlation. The reason is that as the weight of the vehicle increases, the inertia gradually increases. Although the coupling force between the tire and the road surface

caused by vibration increases, its growth rate is smaller than the growth rate of the static axle load.

For the NE-ALT, it increases the axle load by increasing the pressure of the hydraulic cylinder instead of increasing the mass. During this process, the mass of the device has not changed, and its inertia has not changed. At the same time, as the pressure of the hydraulic cylinder increases, the reaction force acting on the frame of the device increases, causing the center of gravity of the device to move upward gradually, as shown in Figure 10. In this case, the dynamic load growth rate of the device is greater than the static load growth rate. Therefore, the change rule of the *DLC* of the device with the axle load is different from that of the actual truck. So the *DLC* also increases with the increase of the hydraulic pressure of the device. When the hydraulic pressure increases from 8.5 MPa to 10.5 MPa, the *DLC* of the device increases from about 0.042 to 0.059.

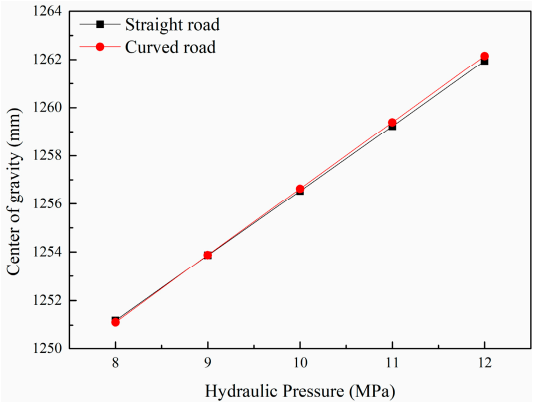

Figure 10. Z coordinate of the center of gravity under different hydraulic pressure.

Fitting and comparing the *DLC* obtained from the measured and the simulated are shown in Figure 11.

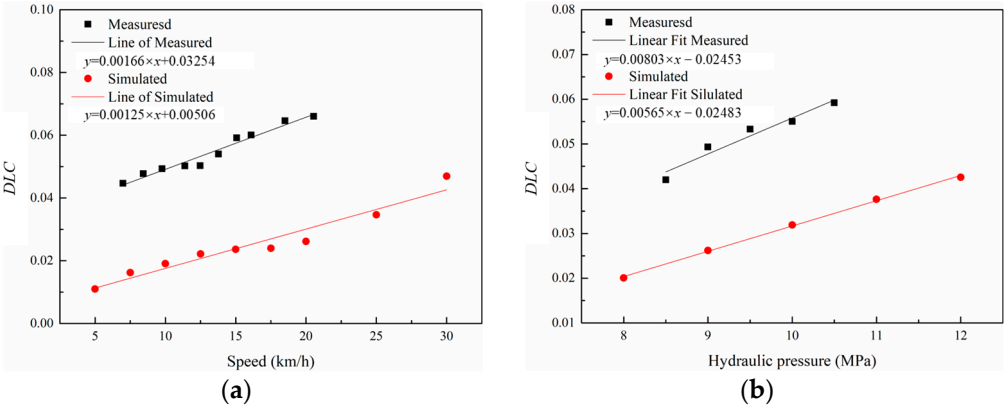

(**a**) (**b**)

Figure 11. Comparison of *DLC* between measured and simulated. (**a**) Different Speeds. (**b**) Different Hydraulic Pressures.

Under different speeds, the measured *DLC* is 0.03 higher than the simulated on average, and the slope values of the two fitting curves are almost the same. Under different hydraulic pressure conditions, the measured *DLC* is 0.02 higher than the simulated on average, which is similar to the different speed conditions, and the slope values of the fitted curves are almost the same. It shows that the *DLC* of the device has a positive correlation with the speed and the hydraulic pressure.

The main reason that the measured *DLC* is greater than the simulated is that the actual piezoelectric units are prestressed by the bolts of packaging, and thus the system's output is not zero when the external load is zero, which will cause the system output to

fluctuate under different external load conditions. At the same time, the system collects a single-point dynamic axle load where the point is in the straight section of the test road, and the simulation test value is obtained by averaging the overall dynamic load of the straight section, so measured data and simulated data deviate. Generally speaking, the simulation dynamic axle load change trend is similar to the actual dynamic axle load, so it can be considered that the virtual prototype model can simulate the dynamic axle load characteristics of the device.

2.3.4. Measurement of Road Roughness

The road roughness is an important part that affects the dynamic axle load. Road engineers usually use the International Roughness Index (*IRI*) to evaluate road roughness, and vehicle engineers usually use Power Spectral Density (*PSD*) to describe road roughness.

The 3 m ruler and feeler gauge, as shown in Figure 12a, was used to measure the road roughness of the circular test road. Figure 12b is a schematic diagram of the circular test road, the straight road section is 40 m long, and continuous measurement is performed without interruption. The radius of the center line of the curved road section is 17 m, and the curved road section is equally divided by 10 degrees, and the chord length of each section is measured continuously.

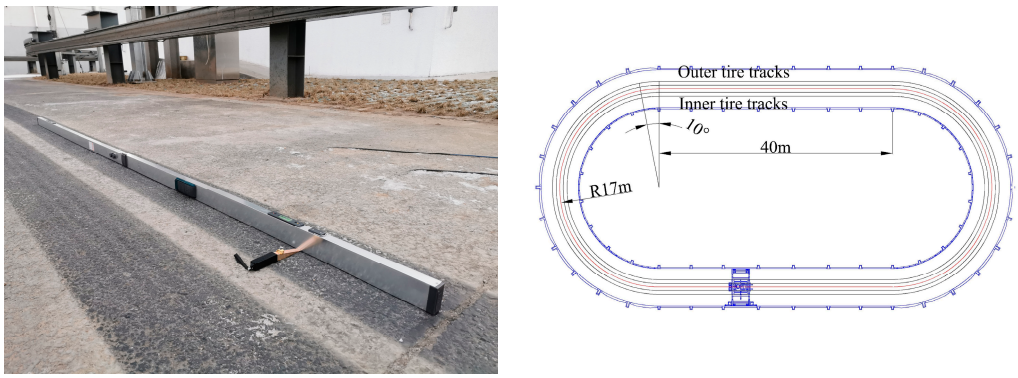

(**a**) (**b**)

Figure 12. Measurement of road roughness. (**a**) 3 m Ruler and Feeler Gauge. (**b**) Circular Test Road.

The 3 m ruler does not directly obtain the *IRI* or *PSD* value but the elevation h of the feeler gauge. The Ministry of Transport of the People's Republic of China has given the conversion relationship between *IRI* and feeler height h as in Equation (9).

$$IRI = 0.3803\,h - 0.4537 \tag{9}$$

The average value of *IRI* is counted every 10 m for straight road sections, and the average value of *IRI* is counted every 30 degrees for curved road sections. There are 20 *IRI* values for the inner and outer wheel tracks, as shown in Figure 13.

Because the road roughness in ADAMS is evaluated by the *PSD* standard, it is necessary to convert the *IRI* value to the *PSD* value. Chen [2] has given the conversion relationship between *PSD* and *IRI* as shown in Equation (10).

$$IRI = 0.78 \times a_0 \times \sqrt{G_q(n_0)} \tag{10}$$

where: $a_0 = 10^3\ \mathrm{m}^{-1.5}$, $G_q(n_0)$ is pavement power spectral density function.

The corresponding relationship between road grade, *PSD*, and *IRI* is shown in Table 3.

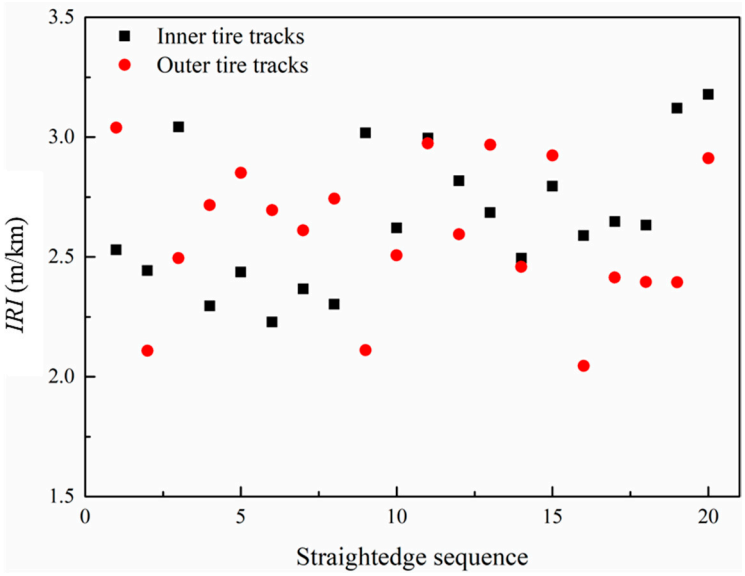

Figure 13. *IRI* Values.

Table 3. The corresponding relationship between road grade, *PSD*, and *IRI*.

Road Grade		A	B	C
G_q (n_0) (10^{-6} m^3)	Lower Limit	8	32	128
	Upper Limit	32	128	512
IRI (m/km)	Lower Limit	2.21	4.42	8.84
	Upper Limit	4.42	8.84	17.64

Combining Table 3 and Figure 12, it can be seen that the road grade of the test road is Grade A, and the same grade should be selected in ADAMS.

3. Results and Analysis

3.1. Effect of Speed on Dynamic Axle Load

The test road roughness grade is A, so this grade is selected, and the static axle load of the device is set to 240 kN. The speeds include 10 km/h, 15 km/h, 20 km/h, 25 km/h, and 30 km/h for analysis. The dynamic performance of the device is very different between straight road sections and curved road sections. Moreover, due to the lack of a gentle curve, the device has a large amplitude of vibration during these sections. The dynamic axle load change caused by this vibration is different from that of the device at a stable road section. Therefore, the unstable sections in the process of entering and exiting the bend are not considered; only the stable section of the curved road section and the stable section of the straight road section are selected for dynamic axle load analysis.

Figure 14 shows the dynamic axle load, *DLC*, and *IM* changing with the speed in curved road sections. The dynamic axle load, *DLC*, and *IM* of the device all increase with the increase in speed. The total dynamic axle load increased from 242.60 kN to 246.39 kN; *DLC* increased from 0.001 to 0.016; *IM* increased from 2.05% to 9.09%. When the vehicle speed reaches 30 km/h, the *IM* value increases significantly. The main reason is that in curved road sections, the device relies on rigid wheel-track contact to swerve, and the change in wheel-track contact force is proportional to the square of the speed. Therefore, as the speed increases, the wheel-track contact force will increase significantly, causing the device to vibrate and the significant changes in the dynamic axle load.

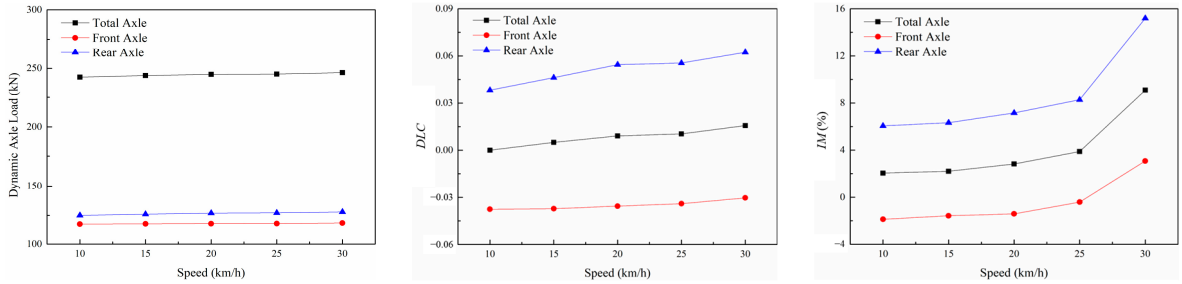

Figure 14. Dynamic axle load in curved road sections with different speeds under simulation conditions. (**a**) Dynamic axle load. (**b**) *DLC*. (**c**) *IM*.

It can be seen from the figure that the *DLC* and *IM* of the front axle are negative, indicating that the dynamic axle load of the front axle is less than the static axle load in the curved road section. The reason is that the contact force between the outer front auxiliary guide wheel and the track provides the device steering centripetal force during the operation in the curved road section. The vertical coordinate of this point is higher than the center of mass, and its force will generate a moment at the center of mass to cause the device to recline. Therefore, in curved road sections, the dynamic axle load of the front axle will be less than its static axle load and will increase as the vehicle speed increases.

Figure 15 shows the dynamic axle load in the straight road section under different speeds. In the straight road section, the dynamic axle load, *DLC*, and *IM* all increase with the increasing speed. Among them, the dynamic axle load increases from 246.45 kN to 254.47 kN, *DLC* increases from 0.016 to 0.049, and *IM* increases from 1.86% to 4.69%.

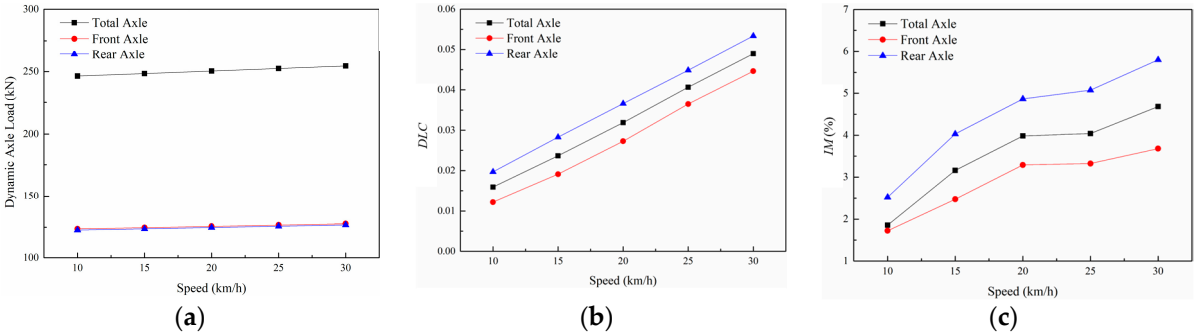

Figure 15. Dynamic axle load in straight road sections with different speeds under simulation conditions. (**a**) Dynamic axle load. (**b**) *DLC*. (**c**) *IM*.

Compared with the curved road section, the dynamic axle load and *DLC* in the straight road section are higher than those of the curved road section, while the *IM* is lower than that of the curved road section. The reason is that the external force acted on the device in the straight section remains stable, the vibration is small, and the force loaded on the rear suspension assembly through the hydraulic cylinder is relatively stable, so its *IM* is small. At the same time, the dynamic axle load and *DLC* have a good correlation with the speed change. The external force in the curved road section always keeps changing, and the wheel-track contact force is much higher than in the straight road section, resulting in poor stability in the curved road section and a large *IM*.

Meanwhile, when the stability of the device is poor, the hydraulic cylinder is affected, and its actual force may decrease compared to static conditions, resulting in the dynamic axle load and *DLC* in the curved road section being lower than that in the straight road section. As shown in Figure 16, the Z-direction force of the hydraulic cylinder under the condition of 20 km/h is extracted with the running distance. Among them, 20–73 m and 113–167 m are curved road sections, and the rest are straight road sections. It can be found

that the force is relatively stable on straight-road sections. Due to device fluctuations in curved road sections, the hydraulic cylinder will slightly rotate around the fulcrum, which causes the actual vertical force of the device in the curved road section to be slightly smaller than that on the straight road section.

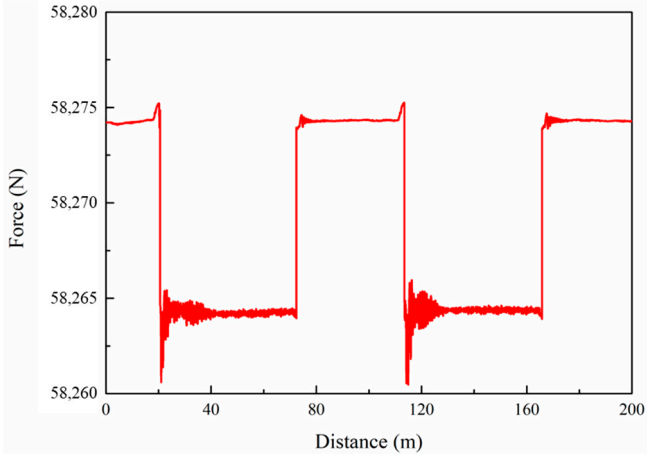

Figure 16. Changes in the Z-direction component force of the hydraulic cylinder during the operation.

3.2. Effect of Hydraulic Pressure on Dynamic Axle Load

In this modeling, the vehicle speed is set to 20 km/h, and the road roughness class is A. The hydraulic pressure is selected to be 8 MPa, 9 MPa, 10 MPa, 11 MPa, and 12 MPa to analyze both the curved road section and the straight road section, respectively. The dynamic axle load in curved road sections under different hydraulic pressures is shown in Figure 17.

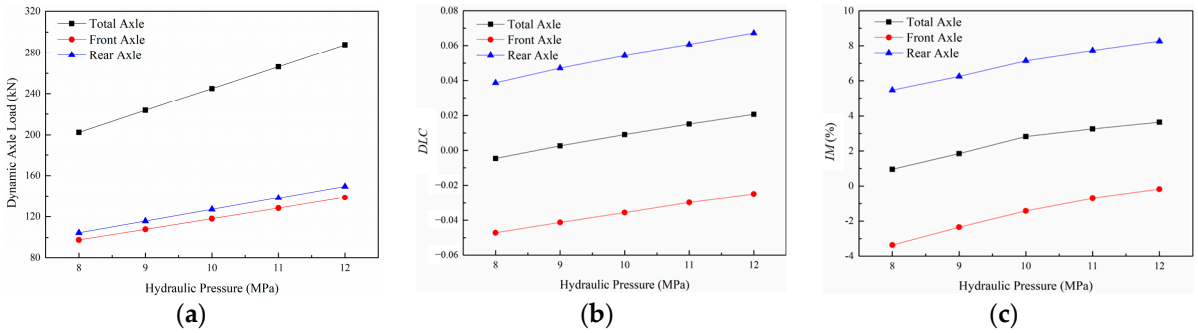

Figure 17. Dynamic axle load in curved road sections with different hydraulic pressure under simulation conditions. (**a**) Dynamic axle load. (**b**) *DLC*. (**c**) *IM*.

It can be seen from the figure that the dynamic axle load, *DLC* and *IM* all increase with the increase of the hydraulic pressure. The total axle load increased from 202.37 kN to 287.87 kN, *DLC* increased from −0.005 to 0.021, and *IM* increased from 0.96% to 3.65%. As mentioned above, because the device is affected by the vibration of the device in the curved road section, the force of the hydraulic cylinder in the running state is not as high as that under static conditions, so the dynamic axle load of the device under the condition of 8 MPa is slightly less than the static axle load.

Figure 18 shows the dynamic axle load in the straight road sections under different hydraulic pressures. The total axle load increased from 207.39 kN to 294.03 kN, *DLC* increased from 0.020 to 0.043, and *IM* increased from 2.64% to 5.11%. Compared with curved road sections, the dynamic axle load, *DLC*, and *IM* of the straight road sections are improved. The dynamic load characteristic evaluation indicators are based on the static axle load. The device runs more smoothly in straight-road sections, so the changes of

various values are more regular. The loading force in curved road sections may be lower than that under static conditions, and all values are decreased compared with those under straight road conditions.

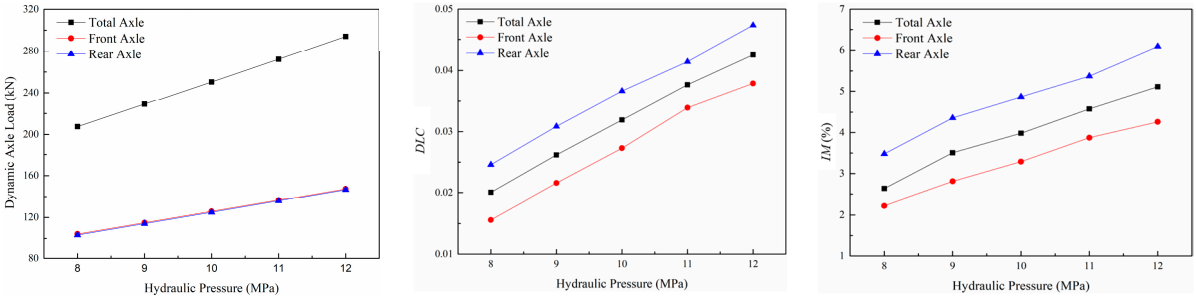

(**a**) (**b**) (**c**)

Figure 18. Dynamic axle load in straight road sections with different hydraulic pressure under simulation conditions. (**a**) Dynamic axle load. (**b**) *DLC*. (**c**) *IM*.

3.3. Effect of Road Roughness on Dynamic Axle Load

The axle load of the device is set at 240 kN, and the vehicle speed is 20 km/h for modeling. The four classes of road roughness under the *PSD* standard of A, B, C, and D are analyzed.

Figure 19 shows the dynamic axle load in the curved road section under different road roughness. The dynamic axle load, *DLC* and *IM* all increase with the increase of the road roughness class. The total axle load increased from 244.91 kN to 250.69 kN, *DLC* increased from 0.009 to 0.028, and *IM* increased from 2.82% to 4.89%. The *IM* change rate in curved road sections increases with the increase of road roughness class, indicating that the increase in road roughness causes the device to vibrate, which leads to an increase in *IM*. At the same time, the *DLC* change rate in the curved road section decreases. The reason is that the device vibration reduces the hydraulic cylinder loading force. Although the dynamic axle load still increases in general, its growth rate becomes smaller and smaller.

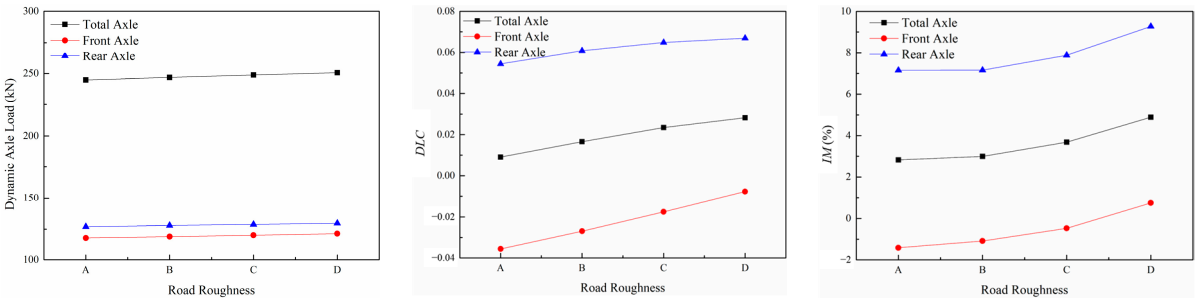

(**a**) (**b**) (**c**)

Figure 19. Dynamic axle load in curved road sections with different road roughness under simulation conditions. (**a**) Dynamic axle load. (**b**) *DLC*. (**c**) *IM*.

Figure 20 shows the dynamic axle load in the straight road sections under different road roughness. The dynamic axle load, *DLC*, and *IM* all increase with the increase of the road roughness class. The total axle load increased from 250.45 kN to 256.17 kN, *DLC* increased from 0.032 to 0.051, and *IM* increased from 3.98% to 6.73%.

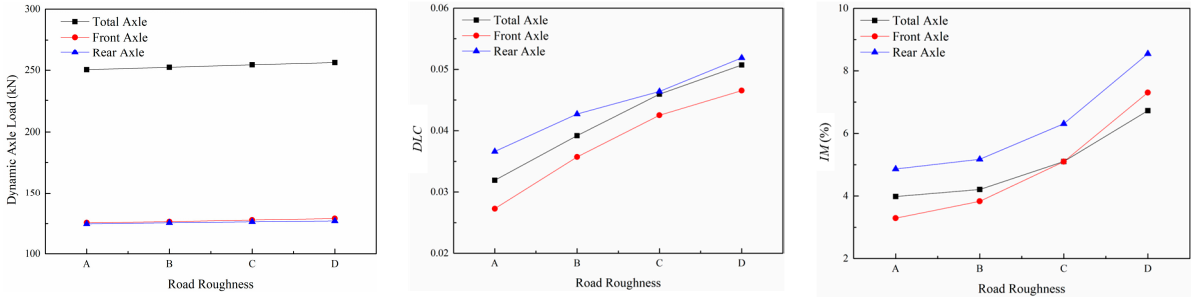

Figure 20. Dynamic axle load in straight road sections with different road roughness under simulation conditions. (**a**) Dynamic axle load. (**b**) *DLC*. (**c**) *IM*.

3.4. Comparison of DLC between Device and Truck

The field test results of Lu et al. [7] were referenced to compare with the Virtual prototype model. In their test, a three-axle truck DFL1250A9 was used, and its two-axle rear axle is similar to the axle used in the NE-ALT, so the test results are used for comparative analysis. The control parameters of the simulation model were set according to its operating conditions. Figure 21 shows the comparison of the virtual prototype model and the truck under different speeds, axle loads, and road roughness conditions. When comparing different speeds, the axle load was full load, and the road roughness class was B; when comparing different axle loads, the speed was 60 km/h, and the road roughness class was B; when comparing different road roughness, the speed was 60 km/h, the axle load was full.

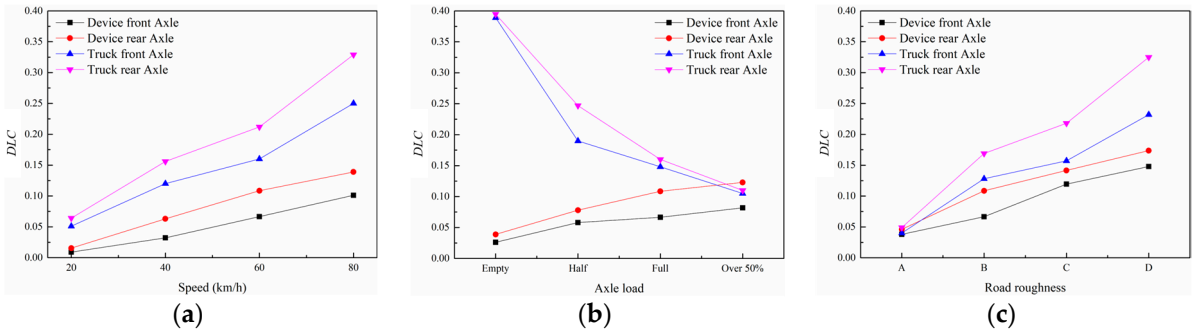

Figure 21. Comparison of *DLC* between device simulation data and truck measured data. (**a**) Speed. (**b**) Axle load. (**c**) Road roughness.

It can be seen from the figure that if the device is under the same working conditions as the truck, its *DLC* is significantly lower than that of the truck, and under different axle load conditions, the variation of *DLC* is opposite to that of the truck. The main reasons include the following:

(1) During the operation of the truck, it is basically in a free state and has no guide track to restrict it. The tracks set on roadsides not only limit the horizontal movement of the device through contact with the guide wheels but also provide support reaction force through contact with the bearing wheels and limit the vertical vibration of the device, thereby reducing the tire coupling force. Therefore, the device *DLC* is always smaller than that of the truck;

(2) The axle load of the truck is increased by increasing the mass of the cargo, and its mass will not be reduced due to the vibration. At the same time, the larger the mass, the stronger the ability to resist external interference, which leads to an increase in the absolute value of the dynamic axle load and a decrease in the rate of change. The device adopts the method that increases the pressure of the hydraulic cylinder to increase the axle load. In fact, the mass of the device is not changed, so its resistance to external forces does not increase. When the hydraulic pressure increases, the larger the reaction force required by

the device and the higher the height of the device's center of mass; therefore, the vibration of the device will increase, causing fluctuations in the dynamic axle load. However, as the device vibrates more severely, it will adversely affect the force actually acting on the rear suspension assembly and reduce it. Therefore, even though the *DLC* of the device is gradually increasing, its growth rate is lower and lower.

4. Discussion

In this study, a virtual prototype model of NE-ALT was constructed using multibody dynamics analysis software, and the reliability of the model was verified. Based on the virtual prototype model, simulation experiments are carried out, and the effects of vehicle speed, hydraulics, and road surface flatness on the dynamic load characteristics of the device are analyzed, and the dynamic load characteristics of the actual vehicle under the same conditions are compared. The results of this study show that the dynamic load factor (*DLC*) of the device NE-ALT varies with different speeds and road roughness, which is similar to actual vehicles. However, its dynamic load factor *DLC* is not affected by the magnitude of the applied shaft load. This is different from real vehicles. This study provides an understanding of the differences in dynamic load characteristics between the equipment and actual trucks.

Scholars in the field of APT mostly focus on the service performance of the pavement under APT equipment and lack of analysis of the difference between APT equipment and real traffic load, which may cause deviation in the evaluation results of pavement service performance. This study analyzes the difference between the dynamic load characteristics of APT equipment and real trucks. It provides a reference for future APT test analysis.

There are still some shortcomings in this study. The pavement model is reduced to a two-dimensional plane, and although the pavement roughness *IRI* parameter was added, there were no pavement material and structural properties. Therefore, it cannot be used to analyze the mechanical response of the pavement under load. During the service of the real pavement model, the pavement roughness index will change, and the interaction model of tires and pavement with different materials and structures is also different.

In future research, the pavement model can be further improved, and the dynamic load characteristics and dynamic pavement response law of APT equipment can be analyzed at the same time. In order for the APT test to evaluate pavement performance more accurately, the characteristics of the loading equipment itself and the interaction between the equipment and the pavement need to be further studied.

5. Conclusions

In this study, based on the multi-body dynamics theory, a virtual prototype model of the Natural Environment-Automatically Loaded Track(NE-ALT) was established. After the analysis of the simulation and field tests, the following conclusions can be made:

(1) According to the field test results, the reliability of the model was verified. By comparing the simulated value with the measured value, the maximum deviation of the speed was 1.81%; The maximum deviation of the total static shaft load was 2.37%, which proved that the model had good reliability;

(2) According to the simulation results, the *DLC* and *IM* of the device bear a positive correlation with the vehicle speed, hydraulic pressure, and road roughness. When the speed is between 10–30 km/h, the maximum *IM* is 9.09%, and the maximum *DLC* is 0.049. When the hydraulic pressure is between 8~12 MPa, the maximum *IM* is 5.11%, and the maximum *DLC* is 0.043. when the road roughness class is between A and D, the maximum *IM* is 6.73%, and the maximum *DLC* is 0.032. These suggest that the dynamic axle load characteristics of the device are most affected by speed, followed by the class of road roughness and then the pressure of the hydraulic cylinder;

(3) According to the comparison between the simulation result of the device and the field test result of a truck, if the device and the truck are under the same operating conditions due to the restraints of the tracks set on roadsides, *DLC* of the NE-ALT is

significantly lower than that of the truck. Under heavy load conditions, the dynamic axle load characteristics of the device are similar to those of the actual vehicle.

The dynamic axle load characteristics are affected by vehicle speed, road roughness, and hydraulic pressure. Therefore, the influence of different operating conditions on the dynamic axle load should be considered in the APT test.

Author Contributions: Conceptualization, L.W.; Data curation, Z.Y.; Formal analysis, H.Y.; Funding acquisition, L.W.; Investigation, X.H.; Methodology, H.Y., X.H. and F.S.; Project administration, F.S.; Supervision, F.S.; Validation, Z.Y.; Writing—original draft, X.H.; Writing—review and editing, H.Y. All authors have read and agreed to the published version of the manuscript.

Funding: This research was funded by The National Key Research and Development Program of China, grant number 2019YFE0117600.

Data Availability Statement: Not applicable.

Acknowledgments: The authors wish to extend their gratitude to all those who contributed to the experiments and creation of this paper, with special thanks to Qian Zhao and Peng Lu.

Conflicts of Interest: The authors declare no conflict of interest.

References

1. Sun, L.; Deng, X. Predicting vertical dynamic loads caused by vehicle-pavement interaction. *J. Transp. Eng.* **1998**, *124*, 470–478. [CrossRef]
2. Chen, H.; He, Z. A Study on Simulation of Road Roughness Based on International Roughness Index. *Highway* **2008**, *12*, 155–160. Available online: https://kns.cnki.net/kcms/detail/detail.aspx?FileName=GLGL200811034&DbName=CJFQ2008 (accessed on 25 November 2022). (In Chinese)
3. Yang, S.; Lu, Y.; Li, S. An overview on vehicle dynamics. *Int. J. Dyn. Control* **2013**, *1*, 385–395. [CrossRef]
4. Abbaspour-Gilandeh, Y.; Rashidi-Mohammadabad, F. Evaluation of dynamic load equations through continuous measurement of some tractor tractive performance parameters. *Int. J. Heavy Veh. Syst.* **2013**, *20*, 222–235. [CrossRef]
5. Zhao, Y.Q.; Bai, L.; Liu, L.A.; Ni, Y.B. Measurement and analysis of dynamic loading of trucks. *J. Hunan Univ.* **2014**, *41*, 129–132. Available online: https://kns.cnki.net/kcms/detail/detail.aspx?FileName=HNDX201411018&DbName=CJFQ2014 (accessed on 25 November 2022). (In Chinese)
6. Zhang, S.; Liu, Y.; Wang, Z.; Li, G.; Chen, S.; Liu, M. Effects of slope and flow depth on the roughness coefficient of lodged vegetation. *Environ. Earth Sci.* **2020**, *79*, 155. [CrossRef]
7. Lu, Y.; Yang, S.; Li, S.; Chen, L. Numerical and experimental investigation on stochastic dynamic load of a heavy duty vehicle. *Appl. Math. Model.* **2010**, *34*, 2698–2710. [CrossRef]
8. Buhari, R.; Rohani, M.M.; Abdullah, M.E. Dynamic Load Coefficient of Tyre Forces from Truck Axles. In *Applied Mechanics and Materials*; Trans Tech Publications, Ltd.: Wollerau, Switzerland, 2013; Volume 405–408, pp. 1900–1911. [CrossRef]
9. Lin, J.-H. Variations in dynamic vehicle load on road pavement. *Int. J. Pavement Eng.* **2014**, *15*, 558–563. [CrossRef]
10. Ka'Ka, S.; Himran, S.; Renreng, I.; Sutresman, O. The pneumatic actuators as vertical dynamic load simulators on medium weighted wheel suspension mechanism. In *Journal of Physics: Conference Series, Volume 962, International Conference on Nuclear Technologies and Sciences (ICoNETS 2017)*; IOP Publishing: Makassar, Indonesia, 2018; Volume 962, p. 012022. [CrossRef]
11. Navarrina, F.; Ramírez, L.; París, J.; Nogueira, X.; Colominas, I.; Casteleiro, M.; Fernández-de-Mesa, J.R. Comprehensive Model for Fatigue Analysis of Flexible Pavements considering Effects of Dynamic Axle Loads. *Transp. Res. Rec.* **2015**, *2524*, 110–118. [CrossRef]
12. Sarkar, A. Numerical comparison of flexible pavement dynamic response under different axles. *Int. J. Pavement Eng.* **2016**, *17*, 377–387. [CrossRef]
13. Jiang, J.; Ni, F.; Gao, L.; Lou, S. Developing an optional multiple repeated load test to evaluate permanent deformation of asphalt mixtures based on axle load spectrum. *Constr. Build. Mater.* **2016**, *122*, 254–263. [CrossRef]
14. Xu, F.; Yang, Q.; Liu, W.; Leng, W.; Nie, R.; Mei, H. Dynamic stress of subgrade bed layers subjected to train vehicles with large axle loads. *Shock. Vib.* **2018**, *2018*, 2916096. [CrossRef]
15. Rys, D. Consideration of dynamic loads in the determination of axle load spectra for pavement design. *Road Mater. Pavement Des.* **2021**, *22*, 1309–1328. [CrossRef]
16. Mshali, M.; Steyn, W.J. Incorporating truck speed effect on evaluation and design of flexible pavement systems. *Int. J. Pavement Res. Technol.* **2020**, *13*, 55–63. [CrossRef]
17. Ye, Z.; Miao, Y.; Zhang, W.; Wang, L. Effects of random non-uniform load on asphalt pavement dynamic response. *Int. J. Pavement Res. Technol.* **2021**, *14*, 299–308. [CrossRef]
18. Yan, G.; Ye, Z.; Wang, W.; Wang, L. Numerical analysis on distribution and response of acceleration field of pavement under moving load. *Int. J. Pavement Res. Technol.* **2021**, *14*, 519–529. [CrossRef]

19. Joumblat, R.; Al Basiouni Al Masri, Z.; Al Khateeb, G.; Elkordi, A.; El Tallis, A.R.; Absi, J. State-of-the-Art Review on Permanent Deformation Characterization of Asphalt Concrete Pavements. *Sustainability* **2023**, *15*, 1166. [CrossRef]
20. Hussain, J.; Wilson, D.J.; Henning, T.F.P.; Alabaster, D. Comparing results between the repeated load triaxial test and accelerated pavement test on unbound aggregate. *J. Mater. Civ. Eng.* **2014**, *26*, 476–483. [CrossRef]
21. Abubeker, W. Ahmed and Sigurdur Erlingsson. Numerical validation of viscoelastic responses of a pavement structure in a full-scale accelerated pavement test. *Int. J. Pavement Eng.* **2017**, *18*, 47–59. [CrossRef]
22. Ling, J.; Wei, F.; Chen, H.; Zhao, H.; Tian, Y.; Han, B. Accelerated pavement testing for rutting evaluation of hot-mix asphalt overlay under high tire pressure. *J. Transp. Eng. Part B Pavements* **2020**, *46*, 04020009. [CrossRef]
23. Lv, S.; Hu, L.; Xia, C.; Wang, X.; Borges Cabrera, M.; Guo, S.; Chen, J. Development of fatigue damage model of asphalt mixtures based on small-scale accelerated pavement test. *Constr. Build. Mater.* **2020**, *260*, 119930. [CrossRef]
24. Zhang, L.; Zhou, X.; Wang, X. Research progress of long-life asphalt pavement behavior based on the riohtrack full-scale accelerated loading test. *Chin. Sci. Bull.* **2020**, *65*, 3247–3258. (In Chinese) [CrossRef]
25. Harvey, J.; Popescu, L. *Rutting of Caltrans Asphalt Concrete and Asphalt-Rubber Hot Mix under Different Wheels, Tires and Temperatures–Accelerated Pavement Testing Evaluation*; University of California: Berkeley, CA, USA, 2000. Available online: http://www.ucprc.ucdavis.edu/PDF/Rutting%20of%20Caltrans%20AC.pdf (accessed on 29 March 2023).
26. Harvey, J.; Bejarano, M.; Popescu, L. Accelerated Pavement Testing of Rutting and Cracking Performance of Asphalt-Rubber and Conventional Asphalt Concrete Overlay Strategies. *Road Mater. Pavement Des.* **2021**, *2*, 229–262. [CrossRef]
27. Yang, H.; Wang, S.; Miao, Y.; Wang, L.; Sun, F. Effects of accelerated loading on the stress response and rutting of pavements. *J. Zhejiang Univ. Sci. A* **2021**, *22*, 514–527. [CrossRef]
28. Ungureanu, D.; Țăranu, N.; Hoha, D.; Zghibarcea, Ș.; Isopescu, D.N.; Boboc, V.; Opri, G.; Scutaru, M.C.; Boboc, A.; Hudi, I. Accelerated testing of a recycled road structure made with reclaimed asphalt pavement material. *Constr. Build. Mater.* **2020**, *262*, 120658. [CrossRef]
29. Li, J.; Zhu, L.; Yu, M.; Zuo, S.; Cui, X.; Liu, P. Long-Term Performance of Recycled Asphalt Pavement with Recycled Engine Oil Bottom Based on Accelerated Loading Test. *Coatings* **2022**, *12*, 522. [CrossRef]
30. Jiang, X.; Titi, H.; Ma, Y.; Polaczyk, P.; Zhang, M.; Gabrielson, J.; Bai, Y.; Huang, B. Evaluating the performance of inverted pavement structure using the accelerated pavement test (APT). *Constr. Build. Mater.* **2022**, *346*, 128489. [CrossRef]
31. Wang, W.; Yan, G.; Zhao, K.; Wang, L. Numerical Simulation and Experimental Measurements of Dynamic Responses of Asphalt Pavement in Dry and Saturated Conditions under Full-Scale Accelerated Loading. *Appl. Sci.* **2022**, *12*, 12291. [CrossRef]
32. Cebon, D. Heavy vehicle vibration—A case study. *Veh. Syst. Dyn.* **1986**, *15* (Suppl. S1), 30–43. [CrossRef]
33. Zhang, Y.; Cai, C.; Shi, X.; Wang, C. Vehicle-induced dynamic performance of frp versus concrete slab bridge. *J. Bridge Eng.* **2006**, *11*, 410–419. [CrossRef]
34. Luo, R.; Shi, H.; Teng, W.; Song, C. Prediction of wheel profile wear and vehicle dynamics evolution considering stochastic parameters for high-speed train. *Wear* **2017**, *392–393*, 126–138. [CrossRef]
35. Farhat, N.; Ward, C.P.; Goodall, R.M.; Dixon, R. The benefits of mechatronically guided railway vehicles: A multi-body physics simulation study. *Mechatronics* **2018**, *51*, 115–126. [CrossRef]
36. Pacejka, H.B.; Bakker, E. The Magic Formula Tyre Model. *Veh. Syst. Dyn.* **1992**, *21* (Suppl. S1), 1–18. [CrossRef]
37. Shi, S.J. Discrete Beam Modeling of the Leaf Spring in Adams and Simulation of Suspension k&c Characteristics for Heavy-Duty Rail. Master's Thesis, Jilin University, Changchun, China, 2012. Available online: https://kns.cnki.net/KCMS/detail/detail.aspx?dbname=CMFD2012&filename=1012368097.nh (accessed on 1 November 2022). (In Chinese)
38. Zhao, Q.; Wang, L.; Zhao, K.; Yang, H. Development of a novel piezoelectric sensing system for pavement dynamic load identification. *Sensors* **2019**, *19*, 4668. [CrossRef] [PubMed]